

MAPPING THE STELLAR STRUCTURE OF THE MILKY WAY THICK DISK AND HALO USING SEGUE PHOTOMETRY

JELTE T. A. DE JONG¹, BRIAN YANNY², HANS-WALTER RIX¹, ANDREW E. DOLPHIN³, NICOLAS F. MARTIN¹, TIMOTHY C. BEERS⁴

Draft version March 13, 2021

ABSTRACT

We map the stellar structure of the Galactic thick disk and halo by applying color-magnitude diagram (CMD) fitting to photometric data from the SEGUE survey. The SEGUE imaging scans allow, for the first time, a comprehensive analysis of Milky Way structure at both high and low latitudes using uniform SDSS photometry. Incorporating photometry of all relevant stars simultaneously, CMD fitting bypasses the need to choose single tracer populations. Using old stellar populations of differing metallicities as templates we obtain a sparse three-dimensional map of the stellar mass distribution at $|Z| > 1$ kpc. Fitting a smooth Milky Way model comprising exponential thin and thick disks and an axisymmetric power-law halo allows us to constrain the structural parameters of the thick disk and halo. The thick-disk scale height and length are well constrained at 0.75 ± 0.07 kpc and 4.1 ± 0.4 kpc, respectively. We find a stellar halo flattening within ~ 25 kpc of $c/a = 0.88 \pm 0.03$ and a power-law index of 2.75 ± 0.07 (for $7 \text{ kpc} \lesssim R_{GC} \lesssim 30 \text{ kpc}$). The model fits yield thick-disk and stellar halo densities at the solar location of $\rho_{thick,\odot} = 10^{-2.3 \pm 0.1} M_{\odot} \text{pc}^{-3}$ and $\rho_{halo,\odot} = 10^{-4.20 \pm 0.05} M_{\odot} \text{pc}^{-3}$, averaging over any substructures. Our analysis provides the first clear in situ evidence for a radial metallicity gradient in the Milky Way's stellar halo: within $R \lesssim 15$ kpc the stellar halo has a mean metallicity of $[Fe/H] \simeq -1.6$, which shifts to $[Fe/H] \simeq -2.2$ at larger radii, in line with the two-component halo deduced by Carollo et al. (2007) from a local kinematic analysis. Subtraction of the best-fit smooth and symmetric model from the overall density maps reveals a wealth of substructures at all latitudes, some attributable to known streams and overdensities, and some new. A simple warp cannot account for the low latitude substructure, as overdensities occur simultaneously above and below the Galactic plane.

Subject headings: Galaxy: structure – Galaxy: disk – Galaxy: halo – stars: statistics

1. INTRODUCTION

Studying the stellar structure of the Milky Way has a long history, as early models based on star counts were already constructed by the likes of Herschel (1785) and Kapteyn (1922). Today we know that four ‘components’ make for a sensible approximate description of the Milky Way stellar body, each with different structural, kinematic and population characteristics: the bulge, the thin and the thick disk, and the stellar halo. Accurate determination of the properties of these components is a difficult undertaking, as it requires surveys with (1) sufficient sky coverage to assess the overall geometry, (2) sufficient depth for mapping stars to ~ 10 to 30 kpc, and (3) sufficient information (e.g., color-based luminosity estimates) to obtain reasonable distance estimates for these stars. Furthermore, the presence of dust in the plane of the disk clouds our view of most of the Galaxy at wavelengths shorter than a few microns. For this reason, most previous efforts to study Milky Way structure at low latitudes have used (near-)infrared data, such as the work by Kent et al. (1991) based on data from the Spacelab

infrared telescope, or more recent work using 2MASS data (e.g. Momany et al. 2006; Reylé et al. 2009) or the GLIMPSE survey (Benjamin et al. 2005). While near-infrared surveys provide the only way of studying the low latitude regions, because they suffer much less from dust extinction, they are currently less sensitive than their optical counterparts and often rely on tracer populations with less accurate distances.

Over the past few years, data from 2MASS (Skrutskie et al. 2006) and the Sloan Digital Sky Survey (SDSS; York et al. 2000; Abazajian et al. 2009) have played a key role in revolutionizing our empirical picture of the stellar components of the Milky Way. As the SDSS survey avoided the Galactic plane, much of the work using SDSS data has focused away from the bulk of the Milky Way's stars to high galactic latitudes. Nonetheless, Jurić et al. (2008) have been able to constrain the structural parameters of the stellar halo and the thin and thick disk. Beyond the global parameters, these surveys have also led to the discovery of substructure in both the stellar disk (Newberg et al. 2002; Ibata et al. 2003; Martin et al. 2004; Bellazzini et al. 2006) and halo (Newberg et al. 2002; Belokurov et al. 2006; Grillmair 2006; Belokurov et al. 2007; Jurić et al. 2008; Bell et al. 2008). This detailed substructure provides information on how the Milky Way formed and evolved; as galaxies assemble through mergers and accretions of smaller systems, these events leave identifiable signatures in their structure and kinematics. This also has cosmological implications, as the structure of the dark halo and the in-

Electronic address: dejong@mpia.de

¹ Max-Planck-Institut für Astronomie, Königstuhl 17, D-69117 Heidelberg, Germany

² Fermi National Accelerator Laboratory, P.O. Box 500, Batavia, IL 60510, United States

³ Raytheon Company, 1151 E Hermans Rd, Tucson, AZ 85756, United States

⁴ Department of Physics & Astronomy and JINA: Joint Institute for Nuclear Astrophysics, Michigan State University, E. Lansing, MI, 48824, USA

teractions with dark subhalos can significantly influence the appearance of a galaxy (e.g. Kazantzidis et al. 2008; Younger et al. 2008).

In this paper we derive a new map of the stellar distribution in the Milky Way, in order to study the large-scale structure of the thick disk and stellar halo. Though covering only the Northern celestial hemisphere, and that only sparsely, this map covers both high and low latitudes and uses rigorously derived stellar distances. This map is based on one of the constituent projects of the extended SDSS survey (SDSS II), SEGUE (Sloan Extension for Galactic Understanding and Exploration; Yanny et al. 2009a), which is an imaging and spectroscopic survey aimed at the study of the Milky Way and its stellar populations. Whereas the main SDSS survey avoided low Galactic latitudes, SEGUE imaging scans go through the Galactic plane (see Figure 1), allowing a ‘picket-fence’ view of the Galaxy at these low latitudes. It is this deep, uniform data set that enables a systematic analysis of stellar structure as function of Galactic latitude and longitude, which we base on color-magnitude diagram (CMD) fitting techniques developed by de Jong et al. (2008). A crucial advantage of an analysis based on CMDs is that they bypass the often ad-hoc and sometimes problematic choices of stellar ‘tracers’ (such as K-dwarfs or F-stars) to delineate the structure. Instead, this procedure results immediately in a mass-density map for stellar population components of, say, different metallicity.

To avoid having to fit the complex stellar population make-up of the thin disk, we in the end consider only stars that are more than 1 kpc away from the Galactic mid-plane, and treat the thin disk as a small perturbation to our results. As SEGUE is a northern hemisphere survey, it stays far away from the Galactic bulge, which can be safely ignored. On the other hand, the resulting maps of stellar mass density in the thick disk and halo allow us to measure the structural parameters of these components. In addition, we show that subtracting a smooth Galactic model reveals a wealth of substructure, especially at low latitudes, which we will study in detail in a forthcoming publication.

The outline of this paper is as follows. Section 2 describes the data used for our analysis, and §3 describes the CMD-fitting techniques we utilize. The resulting stellar distributions are presented in §4, where we also fit smooth Galactic models to them, derive structural parameters, and look at deviations from the best fitting model. Finally, we summarize and discuss our results in §5.

2. SEGUE PHOTOMETRY AND COVERAGE

As part of the SEGUE survey (Yanny et al. 2009a), ten 2.5° -wide scans, crossing the Galactic plane at fixed longitudes, were imaged in five passbands (u , g , r , i , and z ; Gunn et al. 1998, 2006; Hogg et al. 2001). These data are available as part of SDSS Data Release 7 (DR7, Abazajian et al. 2009). An automated data reduction and analysis pipeline produces accurate astrometric and photometric measurements for all detected objects (Lupton, Gunn, & Szalay 1999; Stoughton et al. 2002; Smith et al. 2002; Pier et al. 2003; Ivezić et al. 2004; Tucker et al. 2006), reaching a photometric accuracy of 2% down to $g \simeq 22.5$ and $r \simeq 22$ (Ivezić et al.

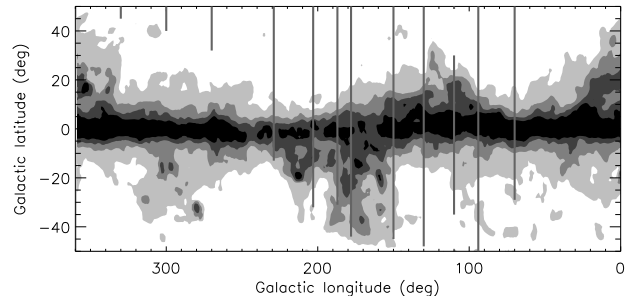


FIG. 1.— Overview of low-latitude imaging scans from SEGUE (Yanny et al. 2009a) used for this analysis, shown as the vertical lines in Galactic coordinates. The grayscale shows dust reddening estimates based on the extinction maps from Schlegel et al. (1998), with increasingly dark regions corresponding to $E(B - V) > 0.1$, 0.25, 0.5 and 1.0 mag. Only regions with $E(B - V) \leq 0.25$ are used in the analysis.

2004; Sesar et al. 2007). Figure 1 shows the coverage of the scans between Galactic latitudes of $+50^\circ$ and -50° . Most scans have some overlap with the SDSS main survey or SDSS Legacy area in the North Galactic cap, and we extract 2.5° -wide strips of data from DR7 to extend the photometry to Galactic latitudes of 85° . For the CMD fitting analysis we restrict ourselves to two bands, g and r . These two bands are the most useful for our population/distance analysis because, among the three photometrically most sensitive bands (g , r and i), they combine to give the largest offset in magnitude between stellar main sequences of different metallicities. The SEGUE imaging in DR7 have been photometrically calibrated following the procedure of Padmanabhan et al. (2008). The procedure basically uses the overlap of the SEGUE data scans with the Legacy SDSS imaging scans to solve for the photometric zero-points and flat-field coefficients of the SDSS 2.5m camera system. This overlap generally occurs in uncrowded regions of sky ($|b| > 20^\circ$) even for scans which extend to cross the Galactic plane. The photometric solution for the SEGUE scans was done incrementally rather than globally after the global solution for all the SDSS Legacy scans. The accuracy of the photometry is estimated to be to about 1.5% in g , and r ($< 2\%$ in color). See §2.2 of Yanny et al. (2009a) for more details on the SEGUE imaging and calibration. We de-redden all data using the dust maps from Schlegel et al. (1998), including the correction suggested by Bonifacio et al. (2000), provided through the SDSS catalog server. As most of the dust is confined close to the Galactic plane, it is in the foreground for all stars more distant than 1 kpc from the mid-plane which we employ in our analysis.

To illustrate the basis for our subsequent modeling, several de-reddened CMDs drawn from different latitudes in the SEGUE stripe at $l=94^\circ$ are shown in Figure 2. The most obvious difference between different latitudes is the variation in reddening, which ranges from an $E(B - V)$ of up to several magnitudes very close to or in the plane of the Galaxy to a few hundredths of a magnitude at high latitudes. Once the reddening reaches several tenths of magnitudes (e.g., the upper right panel of Fig. 2), the unaccounted differential reddening along the line of sight smears out the CMD features. For this reason, and because the dereddening itself is less reliable in high extinc-

tion regions, we exclude regions with $E(B - V) > 0.25$ from our analysis; the excluded regions correspond to the three darkest shadings in Fig. 1. Hence, the two lower panels in Figure 2 are representative for the CMDs used for this study. This cut in foreground extinction also means that we exclude the most crowded regions and thereby avoid possible problems due to crowding.

Before carrying out a more formal CMD analysis, it is instructive to describe the main features seen in the CMDs and to realize which kind of stars they contain. Figure 3 shows the number density of stars in bins in the color-magnitude plane, or Hess diagram, of all stars in the SEGUE scan at $l=94^\circ$ and $b > 30^\circ$. The large concentration of stars in the lower right, i.e. at faint magnitudes and centered at a $g - r$ color of ~ 1.4 consists of nearby, intrinsically faint and low-mass dwarf stars in the disk. The other plume of stars at $g - r \sim 0.4$ is where the main-sequence turn-off (MSTO) stars of old ($\gtrsim 10$ Gyr) stellar populations lie. A shift in the average color of this plume of stars is visible around $g = 18$. This is caused by the difference in metallicity between the thick disk, which dominates at brighter magnitudes, and the Galactic halo, which dominates at larger distances. The color of the MSTO is a useful proxy for the metallicity of the dominant population at a given distance (e.g. see the discussion about this for SDSS isochrones in Girardi et al. 2004). Assuming a regular and smooth Milky Way, the main change between different latitudes are the relative contributions of (thick) disk and halo stars to the CMD. For example, comparing the CMDs corresponding to latitudes of 30° and 70° (lower panels of Fig. 2) shows how the number of disk stars decreases with respect to the halo stars. The field at 70° latitude adds complexity to this description, as it contains an example of stellar substructure; the main-sequence feature produced by the Sagittarius stream is readily visible, running from $(g-r, g) \simeq (0.2, 20.0)$ to $(0.5, 22.0)$.

For our analysis of stellar structure we divide the 2.5° -wide SEGUE stripes into bins of 1° width in latitude from which CMDs are created. Each CMD is then analysed as described in the next Section.

3. DISTANCE FITTING OF CMDs

In most applications of CMD fitting, observed photometry is compared with models in order to determine which combination of simple stellar populations best resembles the data, thereby providing a model of the star formation history (SFH) and age-metallicity relation (AMR). For the work presented here, we fit model stellar population CMDs based on the isochrones in SDSS filters provided by Girardi et al. (2004) to the SEGUE photometry. The software package we use for this (MATCH, Dolphin 1997, 2001) uses a maximum-likelihood method to determine the best linear combination of models, after transforming both models and data to Hess diagrams (2D histograms of stars in the color-magnitude plane), enabling a pixel-by-pixel comparison. For a proper comparison the models need to be convolved with a realistic photometric error and completeness model. The model we use here is the same as in de Jong et al. (2008), based on the photometric errors from the SDSS pipeline (Ivezic et al. 2004) and the completeness determined from a compari-

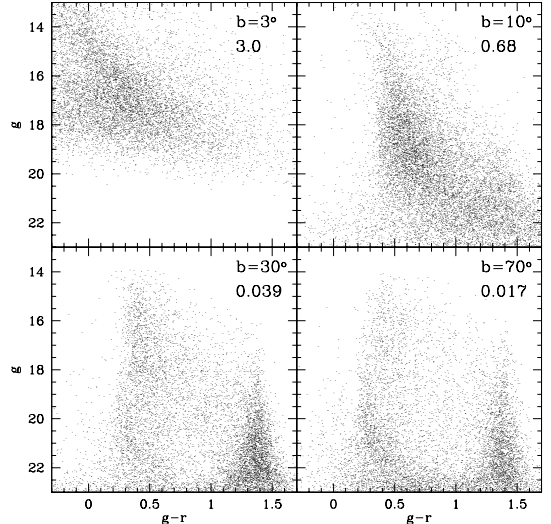


FIG. 2.— Typical color-magnitude diagrams taken from the SEGUE imaging scan at $l=94^\circ$, dereddened based on the dust extinction maps from Schlegel et al. (1998). In the upper right corner of each panel the Galactic latitude and the average reddening in $E(B - V)$ (Schlegel et al. 1998) corresponding to each CMD are indicated. The latitude range from which the CMDs were extracted were chosen so that each contains approximately the same number of stars.

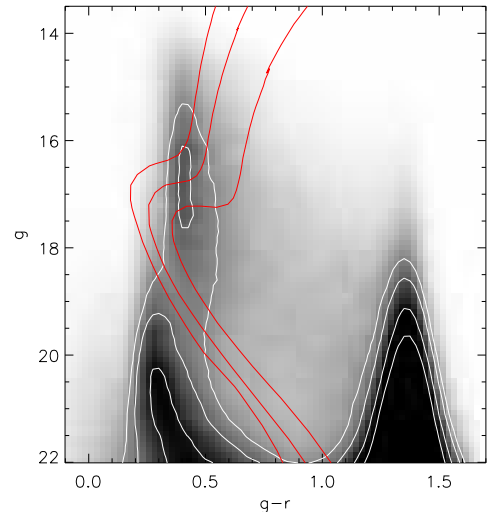


FIG. 3.— A Hess diagram (greyscale) of the SEGUE scan at $l=94^\circ$ and $b > 30^\circ$, in dereddened ($g, g - r$). Overplotted are isochrones corresponding to the three template stellar populations fit to the data. From right to left the isochrones are for the ‘thick-disk-like’ ($[\text{Fe}/\text{H}]=-0.7$), the ‘inner-halo-like’ intermediate metallicity ($[\text{Fe}/\text{H}]=-1.3$) and the ‘outer-halo-like’ metal-poor ($[\text{Fe}/\text{H}]=-2.2$) populations.

son⁵ between SDSS and COMBO-17⁶. Since foreground reddening precludes the use of the most crowded regions in the mid-plane, crowding does not significantly affect the completeness in the data used here.

Rather than determining the SFH and AMR, our aim in the present context is to map the structure of the stellar populations in the inner and outer Milky Way.

⁵ See <http://www.sdss.org/dr5/products/general/completeness.html>

⁶ http://www.mpia.de/COMBO/combo_index.html

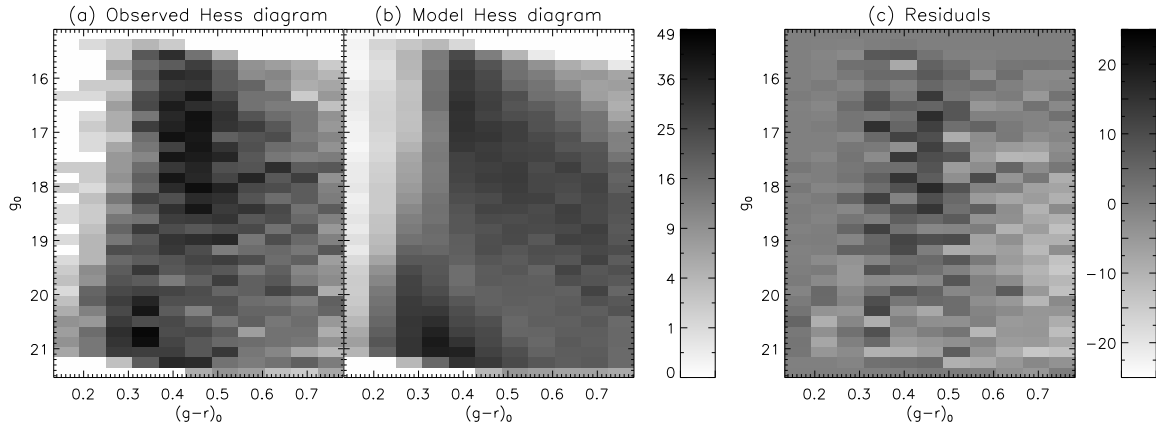


FIG. 4.— Example of distance distribution fitting, based on the Hess/CMD diagram at $l=94^\circ$ and $b=+30^\circ$; note that only the blue portion of the full color range in Figure 3 is shown here. No attempt to model low-mass thin disk stars dominating at $g-r > 0.8$ is made here. (a) Observed distribution of stars in the color-magnitude plane. (b) Best-fit model to (a), consisting of a combination of template stellar populations at different distances. (c) Residuals after subtracting the model (b) from the data (a). Color bars indicate the number of stars in the Hess diagram bins. The mean residuals across the CMD are $\sim 25\%$ of the mean star counts across the entire CMD.

For this, we use the distance-fitting option of MATCH, described and tested in de Jong et al. (2008). To limit the number of free parameters and parameter degeneracy in the fits, we define a small set of template stellar populations. The choice of templates is motivated both by the populations we expect to be present in the outer disk and inner halo, and by the CMD features we have to fit. As discussed in §2, the most obvious indicator of population differences will be the MSTO color, which means the templates should span the expected color range, preferably in regular intervals. The MSTO color of a stellar population depends both on its age and metallicity, but since both the thick disk and the halo stellar populations are known to be old, we choose to use a fixed age range and use metallicity offsets to probe the MSTO color range. We adopt three different metallicity bins, $[\text{Fe}/\text{H}] = -0.7$, -1.3 and -2.2 , respectively. All template populations have the same age range of $10.1 < \log[t/\text{yrs}] < 10.2$, and an assumed binary fraction of 0.5. For convenience, we choose a nomenclature for these components that is based on previous work: we refer to $[\text{Fe}/\text{H}] = -0.7$ as a thick-disk-like population and, following Carollo et al. (2007), refer to the $[\text{Fe}/\text{H}] = -1.3$ and -2.2 templates as the two halo populations, namely, an inner-halo-like and outer-halo-like population, respectively. Note, however, that in our subsequent analysis this choice of terms neither immediately prejudices the geometry, nor implies that these components are ‘distinct’. We simply presume that these three components are sufficient to completely describe the stellar populations at any point that is at least 1 kpc above or below the Galactic mid-plane. Isochrones corresponding to these population templates are overplotted on Figure 3. The colors of the MSTO of populations 1 and 2 match the color of the prominent upper and lower plume of MSTO stars in Figure 3, respectively, while the third population has a bluer MSTO. Using a coarse grid of metallicities means that for stars with a metallicity different from any of the template populations a discrepant distance is inferred, as the brightness of the MS depends is metallicity dependent (see Fig. 3). The magnitude offsets in this case are ~ 0.3 and ~ 0.5 magnitudes, going

from the highest ($[\text{Fe}/\text{H}] = -0.7$) to the lowest metallicity ($[\text{Fe}/\text{H}] = -2.2$) isochrone. As stars with intermediate metallicities will be interpolated between the template populations, this translates into distance uncertainties of at most 10%. The other contributions to the distance uncertainty are inaccuracies in the isochrones and the photometric uncertainties, both of which are expected to be much smaller. The overall distance uncertainty is therefore of order 10%.

We deliberately choose to avoid fitting the thin disk, because a template population with more typical thin-disk populations should have a large range in age and metallicity and would be difficult to distinguish from a combination of the three templates described above. Hence, when presenting and interpreting our results, we will ignore the distance ranges where the thin disk is expected to be an important contribution to the star counts, and only consider regions with $Z > 1.0$ kpc, or roughly four thin-disk scale heights.

All stars with $15 < g < 21.5$, $15 < r < 21.0$ and $0.1 < g-r < 0.8$ are used in the fits, with Hess diagram pixel sizes of 0.07 in color and 0.2 in magnitude. This resolution is sufficient to resolve the features on which the analysis depends, but still ensures sufficient signal-to-noise per pixel. The color-cut of $g-r < 0.8$ eliminates the issue of fitting the faint, red thin-disk stars. For each of the templates, model CMDs are created for a range of distance moduli. The magnitude limits used in the fits ($15 < g < 21.5$) correspond to distance limit for MSTO stars of roughly $1.5 < D < 25$ kpc. Since the MSTO stars provide the best constraints for these CMD fits, only this distance range will be analysed. However, to avoid edge effects, model templates are created for distance moduli between 5.0 (100 pc) to 20.0 (100 kpc) in steps of 0.2 mag ($\sim 10\%$ distance bins). MATCH then determines the best-fitting combination of model CMDs. Subsequently, the uncertainties on the obtained results are determined by refitting Monte Carlo realizations of each CMD drawn from its best-fit model, as described in Dolphin (2001). It is again important to note the difference between this approach and using stars of a particular spectral type to make 3D maps of the Milky Way (as in e.g. Jurić et al.

2008). The CMD fitting will give a direct, high signal-to-noise map of the stellar mass density, even if the stellar populations are spatially varying. This approach also utilizes the information for stars of different spectral types (colors, luminosities) simultaneously.

A comparison of the best-fit model with the CMD data for the region at $l=94^\circ$ and $b=+30^\circ$ (the same field as shown the lower left panel in Figure 2) is presented in Figure 4. Although the model is not perfect (which perhaps should not be expected due to the simple model population make-up), the general features of the density distribution are well-reproduced. The mean residuals are 25% of the mean star counts across the portion of the CMD used in the fit.

4. RESULTS

Rather than the stellar mass or the number of stars, the CMD fitting software provides the star formation rate (SFR) in $M_\odot \text{yr}^{-1}$ corresponding to each population template for each distance modulus bin. However, these SFRs can easily be converted to the spatial stellar mass density using

$$\rho_{*,p} = \frac{3}{\omega(D_2^3 - D_1^3)} \times SFR_p \Delta t, \quad (1)$$

where SFR_p is the star formation rate in $M_\odot \text{yr}^{-1}$ of template population p , Δt is the width of the age bin, ω is the solid angle in steradian corresponding to each CMD, and D_1 and D_2 are the distances corresponding to the limits of the distance modulus bin. The 2001 MATCH version uses a single power-law initial mass function (IMF). In this analysis we opt for a Salpeter IMF (Salpeter 1955) with cutoffs at 0.1 and 120 M_\odot , which yields a total mass of about a factor 2 higher than currently favored IMFs (e.g. Kroupa et al. 1993) for old populations (see also Martin et al. 2008). It should also be kept in mind that these masses correspond to the total mass of stars formed, which, especially for old populations, does not correspond to the total mass in stars today, but rather to the total mass in both stars and stellar remnants.

Figure 5 shows the stellar mass densities obtained from the CMD fits for each of the stripes, summed over all three metallicities. Figure 6 shows the same, but with a color-coding that represents the relative contributions of the three different template populations. Generally speaking, the stellar density decreases in a continuous fashion with increasing distance from the Galactic center and plane, although some deviations are noticeable. For example, a region of apparent excess density extends to the bottom of the $l=94^\circ$ panel in Figure 5, caused by the Sagittarius stream (Majewski et al. 2003; Yanny et al. 2009b). The contributions of the three different template populations change as expected. With increasing distance from the Sun, the ‘thick disk’, ‘inner halo’ and ‘outer halo’ populations dominate in turn. The Galactocentric distance where the metal-poor ‘outer halo’ starts dominating over the more metal-rich inner halo varies between 10 and 20 kpc.

Figure 7 shows the mean density and mass-weighted metallicity as a function of distance from the Sun for a set of different bins in Galactic latitude. Apart from the total mass density, the contributions from the individual template populations are also plotted. The increas-

ing contribution of the thick disk to the density along lines of sight with decreasing latitude is clearly visible, both in the density graphs and in the steepness of the metallicity gradient at distances less than 10 kpc. The metallicity graphs indicate that the stellar halo has an average metallicity of $[\text{Fe}/\text{H}] \simeq -1.6$ at distances less than ~ 15 kpc, confirming the findings of Ivezić et al. (2008), but then drops to $[\text{Fe}/\text{H}] \lesssim -2$ further out. Although the transition is smooth, and both ‘halo-like’ template populations contribute to the mass density at every distance, such a drop is consistent with the presence of two distinct populations, as predicted by Carollo et al. (2007). Recall, however, that the transitions between different templates can only be taken as direct evidence of a metallicity gradient in the halo, if age differences between halo stars play no role in their turn-off color. For the thick disk and stellar halo this is a reasonable assumption, as both are generally believed to be relatively old ($\gtrsim 10$ Gyr), so that the isochrones are much less sensitive to age differences than to metallicity differences.

The stellar density values, $\rho_{*,p}$, are also presented in Table 1. As the table contains 25 476 rows, only the first five rows are printed, with the complete table available in electronic form online.

4.1. Smooth Galactic model fits

To describe the total stellar densities (i.e. summed over all three template populations) quantitatively, we fit a model to all data values $\rho_{*,i}$ represented by the maps in Figure 5. Any substructures that are present on top of a ‘smooth’ stellar distribution should become apparent after subtraction of the best-fit model. The model we use consists of a double exponential thin disk and thick disk (Bahcall & Soneira 1980; Gilmore & Reid 1983), and an axisymmetric power-law halo (Eggen et al. 1962; Chiba & Beers 2000; Jurić et al. 2008):

$$\begin{aligned} \rho(R, Z) = & \rho_{thin,\odot} \left(e^{R_\odot/L_1} \exp\left(-\frac{R}{L_1} - \frac{Z}{H_1}\right) \right. \\ & + f_{thick,\odot} e^{R_\odot/L_2} \exp\left(-\frac{R}{L_2} - \frac{Z}{H_2}\right) \\ & \left. + f_{halo,\odot} \left(\frac{R_\odot}{\sqrt{R^2 + (Z/q_h)^2}} \right)^{n_h} \right). \end{aligned} \quad (2)$$

Here, R_\odot is the distance from the Sun to the Galactic center; L_{thin} , H_{thin} , L_{thick} and H_{thick} are the scale lengths and heights of the thin and thick disk; q_{halo} and n_{halo} are the halo flattening and power-law exponent; $\rho_{thin,\odot}$ is the local thin-disk density and $f_{thick,\odot}$ and $f_{halo,\odot}$ are the local density fraction of the thick disk and halo relative to the thin disk, respectively. In light of the results of Bell et al. (2008) there seems to be no need for a more sophisticated, for example triaxial, halo model. For a grid of parameter values, models are compared to the density values resulting from the CMD fits. Assuming $R_\odot=7.6$ kpc (Vallée 2008)⁷, the distance and the Galactic latitude and longitude of each bin can be converted to R and Z . Since the density in each bin,

⁷ As R_\odot is still not very well determined (e.g. Bovy et al. 2009), we have also used values of 7.1 and 8.1 kpc for R_\odot and found the effects of these changes on the fit results to be negligible compared to the uncertainties quoted in Table 3.

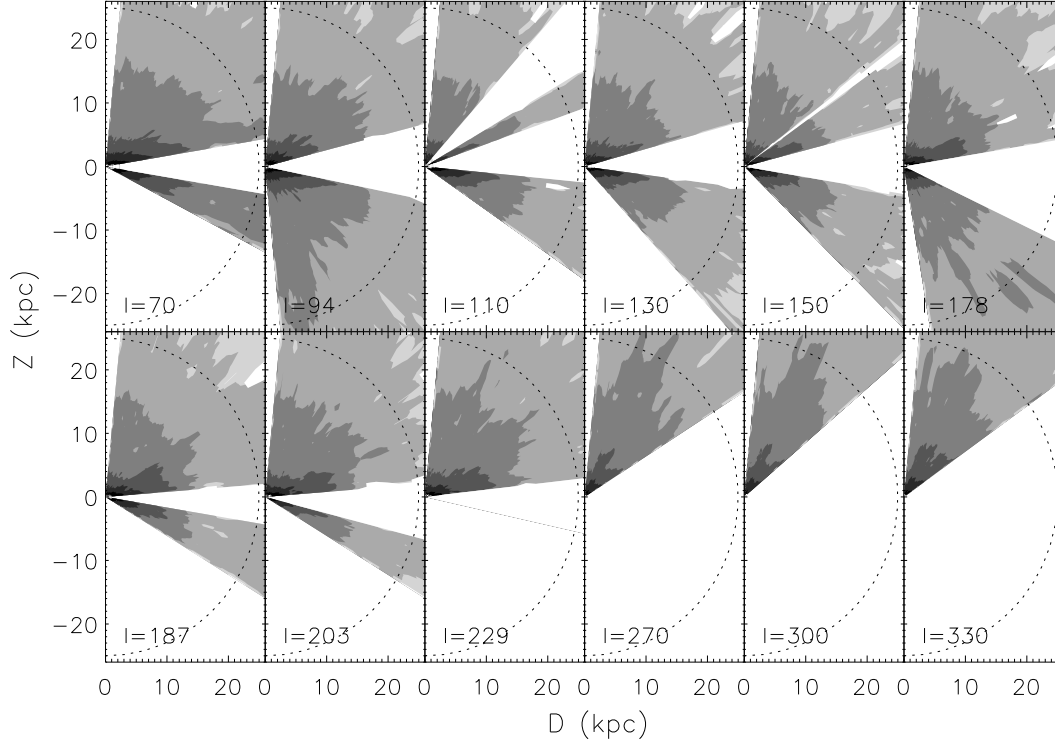


FIG. 5.— Tomography of the Milky Way. Shown are maps of the stellar mass density in a set of slices of constant l , drawing on the single population fits, as function of distance from the Sun, and height above or below the Galactic plane, in kpc. Contours correspond to steps of a factor 10 in stellar mass density. Each panel shows a different imaging scan, the Galactic longitude of which is listed at the bottom, and darker gray levels correspond to higher densities. The dashed semicircles show the maximal distance to which fit results are (mainly) based on main-sequence turn-off star colors and densities.

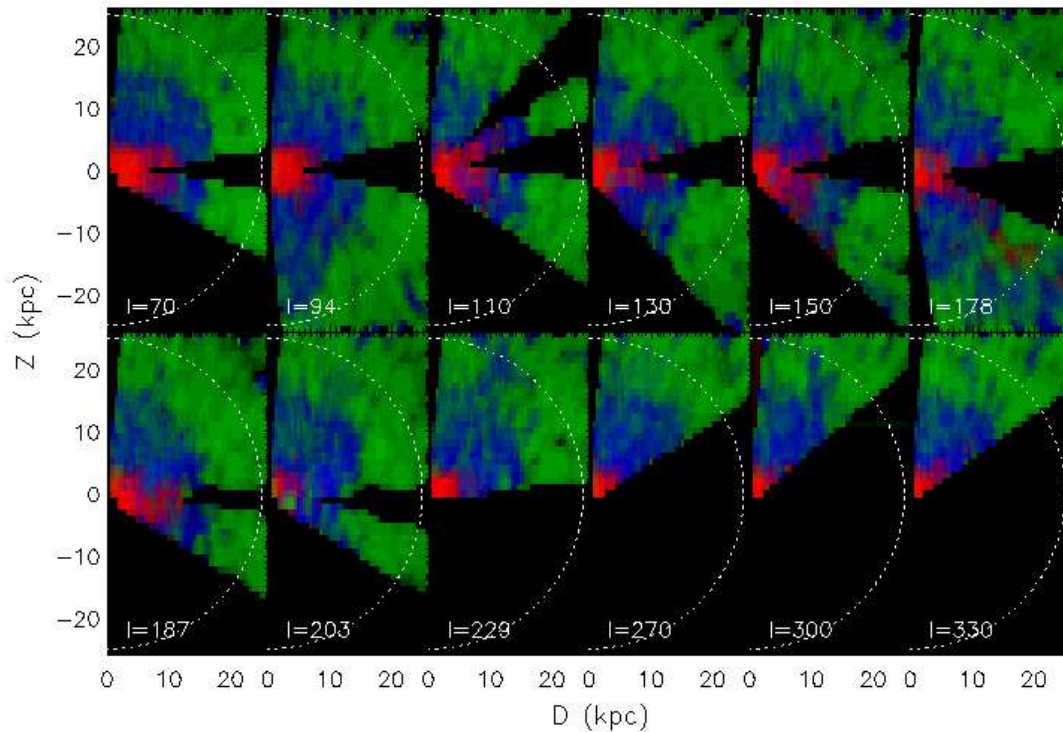


FIG. 6.— Density-metallicity tomography: shown is the distribution of stellar populations from the triple population fits with the same layout as in Fig. 5. The thick-disk-like population with $[\text{Fe}/\text{H}] \simeq -0.7$ is color-coded as red, the inner halo-like population with $[\text{Fe}/\text{H}] \simeq -1.3$ as blue, and the outer halo-like population with $[\text{Fe}/\text{H}] \simeq -2.2$ as green. The white, dashed semicircles show the distance up to where fit results are (mainly) based on main-sequence turn-off star colors and densities.

TABLE 1
STELLAR DENSITY MAPS

l ($^{\circ}$)	b ($^{\circ}$)	m-M (mag)	ρ_1 ($M_{\odot} \text{ kpc}^{-3}$)	σ_{ρ_1} ($M_{\odot} \text{ kpc}^{-3}$)	ρ_2 ($M_{\odot} \text{ kpc}^{-3}$)	σ_{ρ_2} ($M_{\odot} \text{ kpc}^{-3}$)	ρ_3 ($M_{\odot} \text{ kpc}^{-3}$)	σ_{ρ_3} ($M_{\odot} \text{ kpc}^{-3}$)
110.0	-34.5	11.1	0.0	4.76E5	0.0	5.00E3	1.28E7	5.12E6
110.0	-34.5	11.3	0.0	1.16E5	0.0	6.86E5	3.14E6	3.01E6
110.0	-34.5	11.5	0.0	1.51E5	0.0	2.75E5	5.74E6	1.87E6
110.0	-34.5	11.7	1.11E5	1.34E5	0.0	7.00E4	0.0	1.28E6
110.0	-34.5	11.9	2.36E5	2.00E5	0.0	6.49E4	5.1E5	6.46E5

NOTE. — Densities ρ_1 , ρ_2 and ρ_3 correspond to the mass densities for the template populations with $[\text{Fe}/\text{H}]=-2.2$, -1.3 and -0.7 , respectively. The densities in this table correspond to the Salpeter IMF (Salpeter 1955) used by the MATCH software and are in solar masses per cubic kiloparsec, unlike the densities quoted in the text of the paper, which are corrected for a Kroupa IMF (Kroupa et al. 1993) and in solar masses per cubic parsec. This table is available in its entirety in a machine-readable form in the online journal. A portion is shown here for guidance regarding its form and content

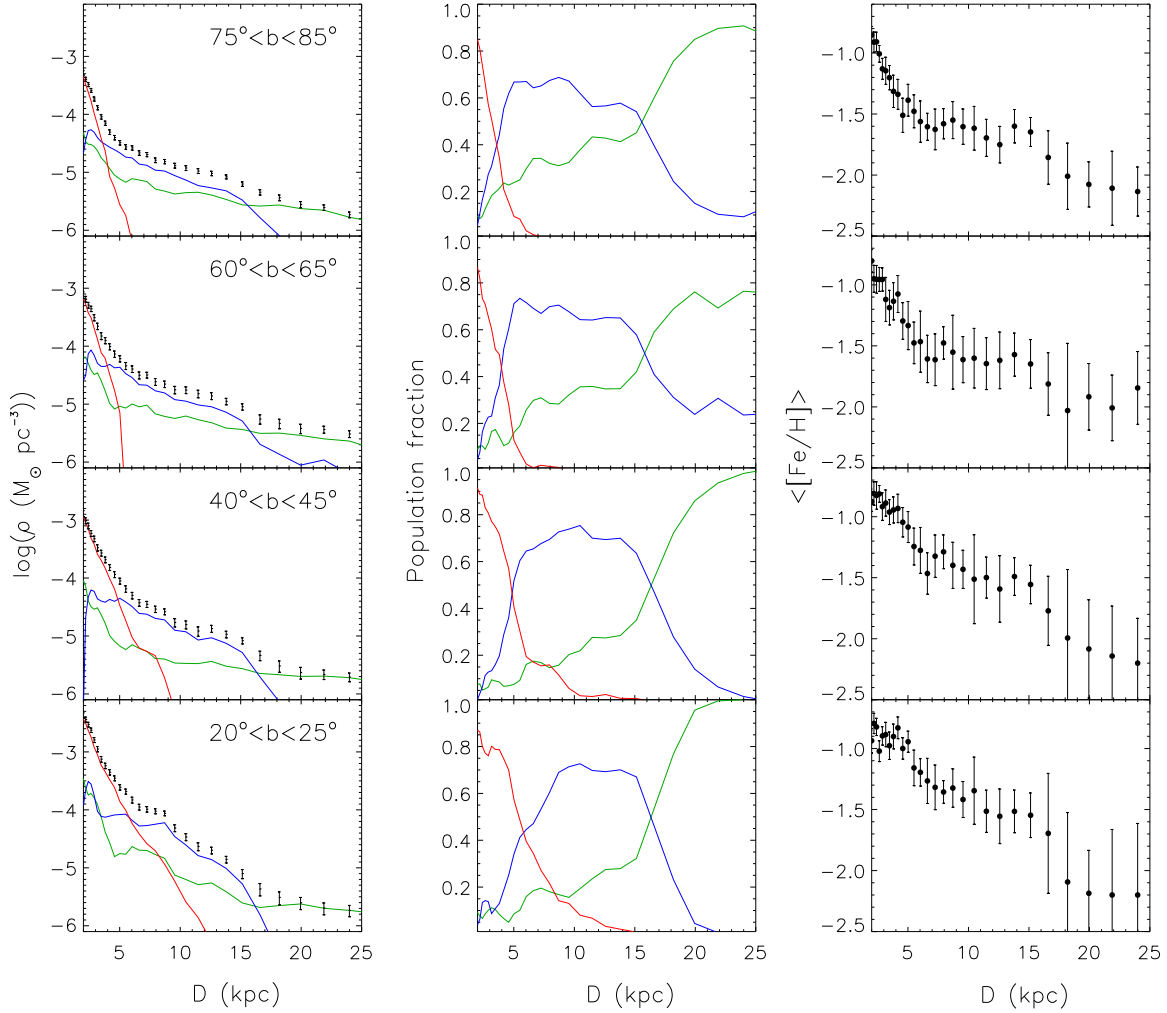


FIG. 7.— Mean stellar mass densities and metallicities as function of distance. The left-hand panels show the total stellar mass density with the black error bars for four different bins in Galactic latitude, indicated in the top right of each panel, and averaged over all longitudes. Colored lines show the mass density in the individual template populations with red for the ‘thick-disk-like’, blue for the ‘inner-halo-like’ and green for the ‘outer-halo-like’ population. In the middle panels the colored lines indicate the fractional contribution of the individual template populations to the total mass density on a scale of 0 to 1, following the same color scheme as in the left-hand panels. The right-hand panels show the mass-weighted mean metallicity.

$\rho_{*,i}(R, Z)$ has an uncertainty from the Monte Carlo tests, the χ^2 goodness-of-fit of each model can be determined straightforwardly as

$$\chi^2 = \sum_i \left(\frac{\rho_{i,model} - \rho_{i,observed}}{\sigma_{i,observed}} \right)^2. \quad (3)$$

As mentioned before, we only use the bins for which $1.5 < D < 25$ kpc and $Z > 1.0$ kpc.

Some localized stellar overdensities are known to exist in the Milky Way which may be strong enough to affect significantly the attempt to fit a ‘smooth’ model. The strongest one in the halo is the Sagittarius stream, presumed to be tidal debris from the Sagittarius dwarf galaxy. It arcs through the North Galactic cap through the stripes at $l=229^\circ$, 270° , 300° , and 330° at high latitudes (Belokurov et al. 2006), and intersects the stripes at $l=94^\circ$ and 178° at negative latitudes (Majewski et al. 2003; Yanny et al. 2009b). This can already be seen in the density maps in Figure 5, for example at $l=94^\circ$, $Z < -15$ kpc and $D < 10$ kpc. At lower latitudes the largest known overdensity is the Monoceros overdensity, discovered by Newberg et al. (2002) and of still controversial origin. It may plausibly be part of the Low Latitude or anti-center stream, a ring-like structure thought to encircle the Milky Way completely (Ibata et al. 2003). This structure can also be seen in Figure 5, near the position of the original discovery (in particular for the $l=178^\circ$ and $l=187^\circ$ stripes, where a ‘bump’ is apparent in the stellar density at $5 < D < 10$ kpc and $0 < Z < 5$ kpc).

To test for the influence of these structures on our fit results, we fit the density maps twice, once with all data, and once without the regions dominated by these structures. The regions that are excised to remove the impact of the Sagittarius stream and Monoceros are listed in Table 2, amounting to $\sim 4\%$ of all data points.

The role of the thin disk is limited by only looking at the area at $|Z| > 1.0$ kpc, and we fix its parameters at $L_{thin}=2.6$ kpc and $H_{thin}=0.25$ kpc, following Jurić et al. (2008) and in line with earlier star count results (e.g Siegel et al. 2002). In other words, we treat the thin disk as a known and fixed ‘perturbation’ to our CMD analysis. We are now left with seven free parameters in fitting the total stellar mass density (summed over the three metallicity components): the thick-disk parameters f_{thick} , L_{thick} and H_{thick} , the halo parameters f_{halo} , q_{halo} and n_{halo} , and the local thin-disk density $\rho_{thin,\odot}$. The latter serves as normalization for the thick disk and halo density, hence in practice reducing the number of free parameters to six.

4.2. Structural parameters of the thick disk and stellar halo

In Table 3 we list the parameter values corresponding to the best fits, with the mass densities scaled to a Kroupa-like IMF (Kroupa et al. 1993). The best fit to all data has a reduced χ^2 of 4.2, while the best fit to the data without Sagittarius and Monoceros has a reduced χ^2 of 3.9. Inclusion of these structures thus has a noticeable impact on the goodness-of-fit, but in both cases the smooth models provide a poor description of the data, in line with Bell et al. (2008) and Jurić et al. (2008). Since this inhibits deriving proper confidence intervals based on the χ^2 statistic, the uncertainties on the

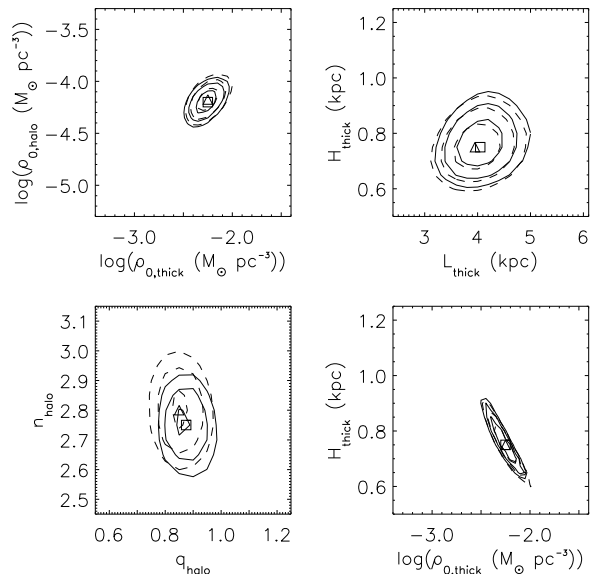


FIG. 8.— Results of fitting smooth Galactic models to the stellar density maps. For the case where all data are used, the best fit values are indicated with squares and iso- χ^2 contours are plotted with solid lines. Triangles and dashed contours are for the case when the Sagittarius stream and the Monoceros overdensity are excised. In both cases, contours are scaled to correspond to the 1, 2 and 3 σ uncertainties determined through bootstrap tests.

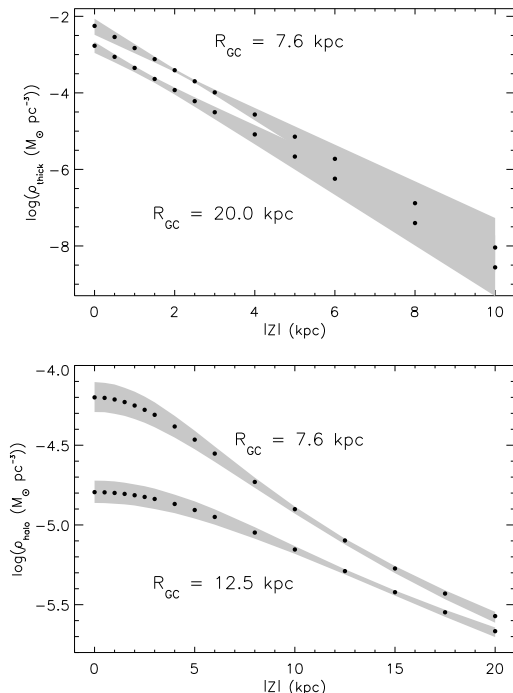


FIG. 9.— Thick disk (top) and halo (bottom) densities in the best-fit smooth model as function of distance from the Galactic plane. The densities were calculated for two galactocentric radii, 7.6 kpc (the assumed galactocentric radius of the Sun) and 12.5 kpc, and the sequences of points are labeled accordingly. Dots show the density at each location for the best-fit model, while the grey areas show the 95% confidence region determined from the bootstrap analysis.

fit parameters listed in Table 3 were obtained by resampling the data points, $\rho_{*,i}(R, Z)$, as in bootstrap tests. For each test, resampled data sets were created by ran-

domly drawing data points (with replacement) from our set of stellar densities, $\rho_{*,i}(R, Z)$, until the same number of data points is reached. The fit parameters were then re-determined for the resampled data sets by re-fitting the model given by Equation 2. This procedure was repeated 200 times for the full data set and for the data set without Sagittarius and Monoceros. In Figure 8 we present the contour plots of the 1σ , 2σ , and 3σ (68%, 95% and 99.7%) confidence levels around the fit parameters, which are also based on the bootstrap analysis.

The mass densities of the thick disk and halo are very well constrained, as demonstrated in Figure 9, where the best model densities and their 95% confidence intervals are plotted at different locations. The thick-disk density is best constrained at $(R_{GC}, |Z|) = (7.6, 2.5)$ kpc as $\rho_{thick} = 10^{-3.70 \pm 0.02} M_{\odot} \text{pc}^{-3}$, and the halo density at $(R_{GC}, |Z|) = (10.0, 12.5)$ kpc as $\rho_{halo} = 10^{-5.19 \pm 0.01} M_{\odot} \text{pc}^{-3}$ ($10^{-5.21 \pm 0.01} M_{\odot} \text{pc}^{-3}$ when Sagittarius and Monoceros are omitted). These formal errors are presumably exceeded by uncertainties in the IMF and associated with substructure. At the solar location the uncertainties on the density are significantly larger than at the locations stated above, as the local values are not directly constrained by the data. Rather, they are extrapolations from data at higher $|Z|$ and R_{GC} , and are therefore model dependent. However, since most previous work has focussed on local samples of stars, we will use the local extrapolations of our results in order to compare with earlier studies. The value we find for the local mass density of the thick disk is $\rho_{thick, \odot} = 10^{-2.3 \pm 0.1} M_{\odot} \text{pc}^{-3}$, and for the stellar halo $\rho_{halo, \odot} = 10^{-4.20 \pm 0.05} M_{\odot} \text{pc}^{-3}$ ($\rho_{thick, \odot} = 10^{-2.3 \pm 0.1} M_{\odot} \text{pc}^{-3}$ and $\rho_{halo, \odot} = 10^{-4.18 \pm 0.05} M_{\odot} \text{pc}^{-3}$ when Sagittarius and Monoceros are omitted).

Recent dynamical modeling (e.g. Flynn et al. 2006) implies a local thick-disk density of $10^{-2.46} M_{\odot} \text{pc}^{-3}$ and a local halo density of $10^{-4} M_{\odot} \text{pc}^{-3}$, similar to our findings. However, our local mass densities include stellar remnants, and a proper comparison should take this into account. The total local mass density, dominated by the thin disk (in stars and white dwarfs), is $\sim 0.038 M_{\odot} \text{pc}^{-3}$ (Flynn et al. 2006). Star-count studies typically yield thick-disk and halo normalizations with respect to the thin disk of 1 to 10% and 0.1 to 0.2%, respectively (Siegel et al. 2002). This therefore implies a local density, including remnants, of $10^{-3.40}$ to $10^{-2.42} M_{\odot} \text{pc}^{-3}$ for the thick disk and $10^{-4.42}$ to $10^{-4.12} M_{\odot} \text{pc}^{-3}$ for the stellar halo, values that are consistent with our density estimates. If we normalize our findings by the local value from Flynn et al. (2006), we find local thick-disk and halo mass-density fractions of $15 \pm 4\%$ and $0.17 \pm 0.03\%$, respectively. Jurić et al. (2008), in their analysis of SDSS data, find $12 \pm 1\%$ for the thick disk, consistent with our results, and $0.51 \pm 0.13\%$ for the halo, inconsistent at the 2.6σ level. These normalizations also imply that the stellar density of the thin disk should never amount to more than $\sim 10\%$ at $|Z| > 1.5$ kpc in our maps, confirming that it is merely a perturbation to our analysis at these locations.

Thick-disk structural parameters determined previously through star-count studies have shown a large spread (e.g. Siegel et al. 2002). Scale heights vary from ~ 0.6 to ~ 2.0 kpc, with the more recent measurements

TABLE 2
REGIONS EXCISED FOR SECOND MODEL FIT

Structure	l ($^{\circ}$)	b ($^{\circ}$)	$m - M$ (mag)
Sgr stream	94	< -65	> 16.0
Sgr stream	178	-65 to -25	> 16.5
Sgr stream	229	$+55$ to $+70$	> 15.5
Sgr stream	270	$+55$ to $+70$	> 15.5
Sgr stream	300	$+58$ to $+72$	> 15.5
Sgr stream	330	$+60$ to $+80$	> 15.5
Monoceros	178	$+15$ to $+35$	14.0–16.0
Monoceros	187	$+15$ to $+35$	14.0–16.0

converging to the lower end of this range; and scale lengths vary from 2.8 to 4.3 kpc. Jurić et al. (2008) find very different values depending on the tracer stars or photometric parallax relations that are used, but settle on 0.9 ± 0.2 kpc and 3.6 ± 0.7 kpc for the thick-disk scale height and length. Through our present analysis we have been able to estimate the scale height and length of the thick disk to 10% accuracy: $H_{thick} = 0.75 \pm 0.07$ kpc and $L_{thick} = 4.1 \pm 0.4$ kpc. This is consistent with but more precise than previous determinations, and in good agreement with the work of Jurić et al. (2008).

Halo parameters, when described by a single power-law, are probably varying with radius (e.g. Bell et al. 2008; Watkins et al. 2009; Sesar et al. 2010), and in this study only the stellar halo within a radius of 25 kpc from the Sun has been considered. Two recent studies based on SDSS data have measured the flattening and power-law index of the stellar halo. Jurić et al. (2008), reaching to ~ 20 kpc, find a halo flattening parameter of $q_h = 0.64$ and a power-law index of $n_h = -2.77$ with quoted uncertainties of $\lesssim 0.1$ and $\lesssim 0.2$, respectively. Bell et al. (2008) find that a q_h of 0.6 to 0.7 gives the least excess rms scatter around their model fits, but that a q_h of 0.7 to 0.8 gives the best χ^2 values. In either case, the constraints on q_h are weak. The halo model used by Bell et al. (2008) is a broken power-law, with independent indices on either side of the break radius. These parameters are also weakly constrained, with the preferred break radius lying between 20 and 30 kpc, the inner power-law index between 2 and 3, and the outer power-law index between 3 and 4. Similarly, Watkins et al. (2009) use RR Lyrae variable stars in SDSS Stripe 82 to infer $n_h = -2.4$ within 23 kpc and $n_h = -4.5$ at larger distances. By comparison, our analysis yields very precise measurements of $n_h = -2.75 \pm 0.07$ and $q_h = 0.88 \pm 0.03$ for the stellar halo within 25 kpc from the Sun. While our value for the power-law index is in excellent agreement with Jurić et al. (2008) and the inner power-law index from Bell et al. (2008), we find the stellar halo to be less flattened. Note that these previous SDSS determinations were restricted to $b \gtrsim 30^{\circ}$; the inclusion of the SEGUE scans across the Galactic plane boosts the power to determine flattening.

4.3. Substructure, or deviations from a smooth model

To focus on substructure in the stellar halo and thick disk we now subtract the best-fit smooth model to the complete data set from the density maps in Figure 5. The residuals after subtracting this smooth model are shown in Figure 10, revealing a wealth of substructure. In par-

TABLE 3
SMOOTH GALACTIC MODEL FITS

Parameter	Full Data	Exclude Sgr, Mon
$\rho_{thick,\odot} (M_{\odot}\text{pc}^{-3})$	$10^{-2.3\pm 0.1}$	$10^{-2.3\pm 0.1}$
L_{thick} (kpc)	4.1 ± 0.4	4.0 ± 0.4
H_{thick} (kpc)	0.75 ± 0.07	0.75 ± 0.08
$\rho_{halo,\odot} (M_{\odot}\text{pc}^{-3})$	$10^{-4.20\pm 0.05}$	$10^{-4.18\pm 0.05}$
q_{halo}	0.88 ± 0.04	0.85 ± 0.03
n_{halo}	-2.75 ± 0.07	-2.80 ± 0.07

ticular, many overdense regions jump out, and although there are also underdense regions, the density contrast of the latter with respect to the smooth model appears to be much weaker. In principle the CMD fitting method can provide not only the stellar densities, but also yield information on the stellar populations of the overdensities, for example their metallicities. However, the current analysis uses three simple template populations, which differ in metallicity but all have the same age (~ 14 Gyr). For the thick disk and stellar halo it is justifiable to interpret the population differences detected in our fits as metallicity differences, as both components consist of old stars. Overdensities, however, might be streams populated by extra-galactic sources or material swept up from even the thin disk. There is no reason to believe that their stars should have the same ages as the smooth components on which they are superposed. The reconstruction of the detailed stellar population properties of specific substructures thus requires a more detailed analysis of each overdensity. Therefore, we limit ourselves here to listing the overdensities we detect and a short description of the main structures responsible for the overdensities seen in Figure 10.

As the strength of an overdensity detection depends on the smooth model that is subtracted from the density maps and each model parameter has a specific uncertainty, we need to define what we consider a significant detection. We do this by constructing a set of smooth Galactic models on a grid of parameters, and selecting all models which are within 1σ of the best-fit model in the 6D parameter space given by the model parameters in Table 3. Density maps are evaluated for all pixels in these 282 models. The pixels with densities at least 3σ higher than the model density for more than half (141) of the models are considered to be significant. Table 4 lists all significantly detected overdensities, most of which consist of a large number of such pixels. The peak significance listed in the table corresponds to the most significant pixel in each overdensity with respect to the best-fit smooth model. The total significance of the overdensity is much larger in most cases, as they consist of many pixels. Because the metallicities and ages of the stars in the overdensities do not necessarily fall neatly within one of the template populations used in the CMD fits, the distances listed should be taken as estimates, not as precise measurements. Note that one detection is caused by two bright globular clusters, NGC 5024 (M53) and NGC 5053, which happen to lie exactly in the scan at $l=330^\circ$.

Sagittarius stream. Probably the most striking stellar ‘substructure’ in the Galactic halo, the Sagittarius stream (labeled with an ‘S’ in Fig. 10) is visible in several

stripes, both in the northern and the southern Galactic hemisphere. The northern arm is clearly visible in the stripes at $l=229^\circ$, 270° , and 300° , just outside the dashed semicircles marking a distance of 25 kpc. At $l=330^\circ$ the stream is more distant (Belokurov et al. 2006) and off the plot. The two arms in which this part of the stream is split (Belokurov et al. 2006) are detected very clearly, particularly in the $l=270^\circ$ stripe. Typical peak densities in these stripes are 5 to $8\times 10^{-6}M_{\odot}\text{pc}^{-3}$. At $l=203^\circ$ the northern Sgr stream should enter the stripe around $b=30^\circ$ and plunge into the disk (Belokurov et al. 2006; Yanny et al. 2009b). As it is roughly equidistant with the Low-Latitude Stream, it is difficult to distinguish it in the overdensity at low latitudes in this stripe. In the southern Galactic cap, the Sgr stream yields strong detections in two stripes, namely the $l=94^\circ$ and 178° stripes, reproducing the detection by Yanny et al. (2009b). Here the stream is also seen at distances of 20 kpc and higher. The density of the stream in these southern detections peaks at $\sim 1\times 10^{-5}M_{\odot}\text{pc}^{-3}$, slightly higher than in the North Galactic cap.

Virgo. The Virgo overdensity (Jurić et al. 2008) is another strong overdensity in the Northern Galactic cap, centered at $(l,b)\simeq(280^\circ,70^\circ)$ and extending between distances of ~ 10 to ~ 20 kpc (Bell et al. 2008; Jurić et al. 2008). It is very prominent in the residual maps of the stripes at $l=270^\circ$ and 300° in the same direction as the Sgr stream, but at distances less than 20 kpc. The overdensities at similar distances in the $l=330^\circ$ stripe might be related to Virgo as well. Typical densities in the Virgo overdensity we find in the $l=270^\circ$ and 300° stripes are $\sim 2\times 10^{-5}M_{\odot}\text{pc}^{-3}$, peaking at around $\sim 4\times 10^{-5}M_{\odot}\text{pc}^{-3}$.

Hercules-Aquila. A large overdensity extending both above and below the disk, and spanning $\sim 80^\circ$ in longitude, was detected by Belokurov et al. (2007) and christened the Hercules-Aquila cloud. This structure is centered at $l\simeq 40^\circ$, but is visible out to $l\lesssim 90^\circ$ (Belokurov et al. 2007). The overdensities detected in the stripe at $l=70^\circ$ and distances larger than ~ 22 kpc might therefore be associated with this recently discovered stellar component.

Monoceros and Low Latitude Stream. The Monoceros structure was first discovered in SDSS data by Newberg et al. (2002) as a strong stellar overdensity at $(l,b)\simeq(200^\circ,20^\circ)$. Later such overdensities were detected over a large range of Galactic longitudes both above and below the Galactic plane, always at low latitudes and roughly equidistant, thus forming a ring-like structure around the Milky Way (Ibata et al. 2003; Yanny et al. 2003; Conn et al. 2005, 2007). In the stripes at the longitudes close to the original discovery, $l=178^\circ$, 187° , 203° and 229° , the overdensity is detected at high significance at heliocentric distances of roughly 10 kpc and ~ 3 kpc above the Galactic plane. The ring-like nature of the Low Latitude Stream appears to be confirmed by our new map, as overdensities at the same heliocentric distances and latitudes are present in the stripes at $l=94^\circ$, 130° and 150° , but not at $l=110^\circ$. The density of the structure is highest in the stripes at $l=178^\circ$, 187° , and 203° , where the maximum density reached is $\sim 1.5\times 10^{-4}M_{\odot}\text{pc}^{-3}$. The density appears to fall off by a factor of ~ 2 in the stripes at both lower and higher longitudes. The overdensity detections at negative lati-

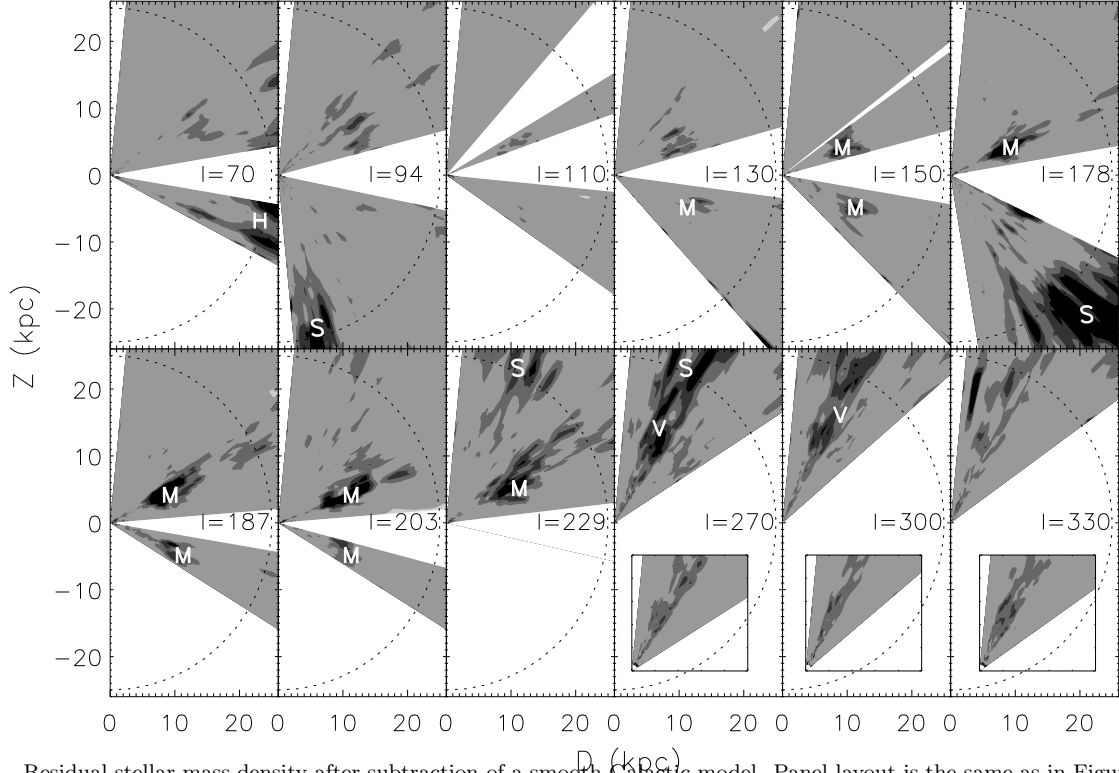


FIG. 10.— Residual stellar mass density after subtraction of a smooth Galactic model. Panel layout is the same as in Figure 5. Starting from black, the grayscale levels correspond to areas with residual densities > 3 , $3-2$, $2-1$, 1 to -1 , and < -1 times the model density. White areas contain no information due to an absence of data or too high reddening. The dashed semicircles show the distance up to where fit results are (mainly) based on main-sequence turn-off star colors and densities. Four known overdensities are labeled: the Sagittarius stream (S), the Virgo overdensity (V), the Hercules-Aquila cloud (H), and the Monoceros, or Low Latitude stream (M). The panels for $l=270^\circ$, 300° and 330° have insets showing the inner 5×5 kpc region.

tudes (Ibata et al. 2003; Conn et al. 2005, 2007) are confirmed here, with an overdensity detected consistently ~ 4 kpc below the plane from $l=130^\circ$ to $l=203^\circ$. Below the plane the overdensities have lower densities than above the plane, increasing from $\sim 0.2 \times 10^{-4} M_\odot \text{pc}^{-3}$ at $l=130^\circ$ to $\sim 1.3 \times 10^{-4} M_\odot \text{pc}^{-3}$ at $l=130^\circ$.

Detection at $(R, Z) = (6.5, 1.5)$. Jurić et al. (2008) detected an overdensity at Galactocentric coordinates $(R, Z) = (6.5, 1.5)$ kpc. In the stripes at $l=270^\circ$, 300° and 330° we find a very nearby overdensity at $b \simeq 65^\circ$ and at a distance range from 4 kpc to the smallest distance we probe, 1.5 kpc. This overdensity therefore corresponds to the same as detected by Jurić et al. (2008). The nature of this overdensity is so far unknown.

Unknown substructure. In a few locations less prominent substructures are visible, that cannot directly be identified with known overdensities. Most of these are located at low latitudes and might be related to the Low Latitude Stream. In a future publication we will study these overdensities and their possible connection with the Low Latitude Stream in detail.

5. SUMMARY AND CONCLUSIONS

We have applied CMD-fitting techniques to SEGUE photometric data to study the thick disk and stellar halo of the Galaxy at both high and low latitudes. Three template stellar populations, all with an age of ~ 14 Gyr and metallicities of $[\text{Fe}/\text{H}] = -0.7$, -1.3 and -2.2 , are fit to the data, yielding a three-dimensional census of stellar mass. Since the thick disk and stellar halo consist of predominantly very old stars, differences in turn-off

color are indicative of differences in metallicity. A change of turn-off color is seen in the halo at distances of 15 to 20 kpc, which is therefore interpreted as a change in metallicity. At distances smaller than ~ 10 kpc our results indicate a mean metallicity of $[\text{Fe}/\text{H}] \sim -1.6$, similar to the work by Ivezić et al. (2008), who find a value of $[\text{Fe}/\text{H}] \sim -1.5$ out to ~ 9 kpc. At larger distances, $D \gtrsim 15$ kpc, our results indicate that the mean metallicity of the stellar halo is $[\text{Fe}/\text{H}] \sim -2.2$, however. This transition is consistent with the inference from local samples of stars ($D \lesssim 4$ kpc) by Carollo et al. (2007) and preliminary results from Beers et al. (2009), but this is the first time this change in population properties is measured *in situ*.

Structural parameters of the Galaxy can be derived from the resulting stellar-density maps through the comparison with models. Our fits of models with an exponential thin and thick disk and a power-law halo (Eq. 2) yield constraints on the thick disk local density, $\rho_{\text{thick}, \odot}$, scale height, H_{thick} , and scale length, L_{thick} , and the halo local density, $\rho_{\text{halo}, \odot}$, flattening, q_{halo} and power-law index, n_{halo} . As pointed out by Belokurov et al. (2006), Bell et al. (2008), and Jurić et al. (2008), the SDSS data of the stellar halo contains clear evidence of the presence of substructure with respect to smooth halo models. Bell et al. (2008) also demonstrated that the larger known substructures in the halo significantly influence their model fits. To test the sensitivity of our model fits to known substructure, we perform our fits to the full data set, as well as to a data set with the Sagittarius stream and Monoceros overdensity removed. The results

TABLE 4
DETECTED OVERDENSITIES

l ($^{\circ}$)	b ($^{\circ}$)	D (kpc)	σ_{peak}	ID
70	(−23,−21)	(14,16)	5.7	
70	(+36,+38)	(15)	8.5	
70	(−23,−22)	(22,25]	4.8	Hercules-Aquila?
70	(−13,−10]	(23,25]	3.4	Hercules-Aquila?
70	[+10,+12)	(23,25]	3.5	Hercules-Aquila?
94	(−82,−70)	(21,25]	6.7	Sgr stream
94	(+18,+22)	(12,14)	4.1	
94	(+32,+35)	(14,16)	8.4	
130	(−18,−16)	(13)	4.2	
130	(+19,+22)	(8,13)	4.7	
130	(+26,+27)	(9)	7.1	
130	(+35,+37)	(9,13)	5.0	
150	(−31,−21)	(11,14)	3.9	
150	(+17,+29)	(8,13)	140	Monoceros
178	(−62,−39)	(22,25]	6.2	Sgr stream
178	(−59.5)	(14)	3.1	
178	(−48,−46)	(11.5)	3.5	
178	(−42,−40)	(12.5)	3.2	
178	(−30,−26]	(11,15)	8.3	
178	(+16,+32)	(5,14)	9.7	Monoceros
187	(−30,−17)	(8,13)	5.7	
187	(+14,+35)	(6,15)	13.1	Monoceros
203	(−28,−15]	(8.5,13)	8.5	Monoceros
203	(+14,+31)	(7,15)	22	Monoceros
203	(+21.5)	(20)	3.3	
229	(+15,+40)	(7,18)	7.1	Monoceros
229	(+35,+38)	(21,24)	6.5	
229	(+57,+64)	(23,25]	4.2	Sgr stream
270	(+58,+69)	(23,25]	4.1	Sgr stream
270	(+55,+74)	(2,23)	8.8	Virgo/(6.5,1.5)
300	(+65,+70)	[1.5,4)	5.4	(6.5,1.5)
300	(+58,+72)	(10,19)	16.1	Virgo
300	(+60,+65)	(21,25]	4.1	Virgo/Sgr stream
330	(+57,+72)	[1.5,4)	5.5	(6.5,1.5)
330	(+55,+73)	(12,24)	7.2	Virgo
330	(+78,+81)	(16.5,22)	12.2	NGC5024/NGC5053

NOTE. — For Galactic latitude b and distance D ranges are given within brackets, with square brackets indicating an edge of the data rather than the edge of a detection.

are tabulated in Table 3, and are not strongly influenced by the presence of these structures. In either case, the reduced χ^2 of the best fit, 4.2 and 3.9, shows that the smooth model is a poor fit to the data.

The values we find for the local density of the thick disk, $\rho_{thick,\odot} = 10^{-2.3\pm 0.1} M_{\odot}\text{pc}^{-3}$ and the local halo density, $\rho_{halo,\odot} = 10^{-4.20\pm 0.05} M_{\odot}\text{pc}^{-3}$, agree well with star-count studies. In addition, our results for the thick-disk structural parameters, $H_{thick} = 0.75 \pm 0.07$ kpc and $L_{thick} = 4.1 \pm 0.4$, are well within the range of parameters found in previous studies (Siegel et al. 2002) and consistent with the results of Jurić et al. (2008). For the flattening of the stellar halo, where we find $q_{halo} = 0.88 \pm 0.04$, our analysis seems to diverge from the work by Bell et al. (2008) and Jurić et al. (2008), who use SDSS data to study the halo out to similar distances. On the other hand, the power-law index we recover, $n_{halo} = -2.75 \pm 0.07$, is in excellent agreement.

Subtracting the best model from the stellar-density maps unveils abundant substructure (Fig. 10). Most of the overdensities seen can be attributed to known structures in the halo and outer disk of the Galaxy: the Sagittarius stream, Virgo overdensity, and the Monoceros overdensity or Low Latitude Stream. Whereas the origin of the Sagittarius stream is known to be the result of the disruption of the Sagittarius dwarf galaxy, the nature of the other two entities is currently under debate, in particular the interpretation of the overdensities at low Galactic latitudes remains contentious. A detailed analysis of all substructures is outside the scope of this paper, but an in-depth study of the low latitude substructure is planned to be presented in a future publication.

The authors thank Eric Bell and Constance Rockosi for stimulating and helpful conversations and Sergey Koposov for logistical help. We are also grateful for helpful comments and feedback from Željko Ivezić and Mario Jurić. J.T.A.d.J was supported by DFG Priority Program 1177. T.C.B. acknowledges partial support for this work from grant PHY 08-22648: Physics Frontier Center/Joint Institute for Nuclear Astrophysics (JINA), awarded by the U.S. National Science Foundation.

Funding for the SDSS and SDSS-II has been provided by the Alfred P. Sloan Foundation, the Participating Institutions, the National Science Foundation, the U.S. Department of Energy, the National Aeronautics and Space Administration, the Japanese Monbukagakusho, the Max Planck Society, and the Higher Education Funding Council for England. The SDSS Web Site is <http://www.sdss.org/>.

The SDSS is managed by the Astrophysical Research Consortium for the Participating Institutions. The Participating Institutions are the American Museum of Natural History, Astrophysical Institute Potsdam, University of Basel, University of Cambridge, Case Western Reserve University, University of Chicago, Drexel University, Fermilab, the Institute for Advanced Study, the Japan Participation Group, Johns Hopkins University, the Joint Institute for Nuclear Astrophysics, the Kavli Institute for Particle Astrophysics and Cosmology, the Korean Scientist Group, the Chinese Academy of Sciences (LAMOST), Los Alamos National Laboratory, the Max-Planck-Institute for Astronomy (MPIA), the Max-Planck-Institute for Astrophysics (MPA), New Mexico State University, Ohio State University, University of Pittsburgh, University of Portsmouth, Princeton University, the United States Naval Observatory, and the University of Washington.

REFERENCES

- Abazajian, K. N., Adelman-McCarthy, J. K., Agüeros, M. A., Allam, S. S., Allende Prieto, C., et al. 2009, *ApJS*, 182, 543
Bahcall, J. N. & Soneira, R. M. 1980, *ApJS*, 44, 73
Beers, T. C., An, D., Johnson, J. A., Pinsonneault, M. H., Terndrup, D. M., Delahaye, F., Lee, Y. S., Masseron, T., et al. 2009, [arXiv:0910.4731](https://arxiv.org/abs/0910.4731)
Bell, E. F., et al. 2008, *ApJ*, 680, 295
Bellazzini, M., Ibata, R. A., Martin, N., Lewis, G. F., Conn, B., Irwin, M. J., 2006, *MNRAS*, 366, 865
Belokurov, V., et al. 2006, *ApJ*, 642, L137
Belokurov, V., et al. 2007, *ApJ*, 657, L89
Benjamin, R. A., Churchwell, E., Babler, B. L., Indebetouw, R., Meade, M. R., et al. 2005, *ApJ*, 630, L149
Bonifacio, P., Monai S. & Beers, T. C.,

- Bovy, J., Hogg, D. W. & Rix, H.-W. 2009, *ApJ*, 704, 1704
 Carollo, D., et al. 2007, *Nature*, 450, 1020
 Chiba, M. & Beers, T. C. 2000, *AJ*, 119, 2843
 Conn, B. C., Lewis, G. F., Irwin, M. J., Ibata, R. A., Ferguson, A. M. N., Tanvir, N. & Irwin, J. M., 2005, *MNRAS*, 362, 475
 Conn, B. C., et al. 2007, *MNRAS*, 376, 939
 de Jong, J. T. A., Rix, H.-W., Martin, N. F., Zucker, D. B., Dolphin, A. E., Bell, E. F., Belokurov, V. & Evans, N. W., 2008, *AJ*, 135, 1361
 Dolphin, A. E. 1997, *New A*, 2, 397
 Dolphin, A. E. 2001, *MNRAS*, 332, 91
 Eggen, O. J., Lynden-Bell, D. & Sandage, A. R. 1962, *ApJ*, 136, 748
 Flynn, C., Holmberg, J., Portinari, L., Fuchs, B. & Jahreiß, H. 2006, *MNRAS*, 372, 1149
 Gilmore, G. & Reid, N. 1983, *MNRAS*, 202, 1025
 Girardi, L., Grebel, E. K., Odenkirchen, M., & Chiosi, C. 2004, *A&A*, 422, 205
 Grillmair, C. J. 2006, *ApJ*, 651, L29
 Gunn, J.E. et al. 1998, *AJ*, 116, 3040
 Gunn, J.E. et al. 2006, *AJ*, 131, 2332
 Herschel, W. 1785, *RSP*, 75, 213
 Hogg, D.W., Finkbeiner, D.P., Schlegel, D.J., & Gunn, J.E. 2001, *AJ*, 122, 2129
 Ibata, R. A., Irwin, M. J., Lewis, G. F., Ferguson, A. M. N. & Tanvir, N. 2003, *MNRAS*, 340, L21
 Ivezić, Ž. et al. 2004, *AN*, 325, 583
 Ivezić, Ž. et al. 2008, *ApJ*, 684, 287
 Jurić, M., et al. 2008, *ApJ*, 673, 864
 Kapteyn, J. C. 1922, *CMWCI*, 230, 1
 Kazantzidis, S., Bullock, J. S., Zentner, A. R., Kravtsov, A. V. & Moustakas, L. A., 2008, *ApJ*, 688, 254
 Kent, S. M., Dame, T. M. & Fazio, G. 1991, *ApJ*, 378, 131
 Kroupa, P., Tout, C. A. & Gilmore, G. 1993, *MNRAS*, 262, 545
 Lupton, R., Gunn, J., & Szalay, A. 1999, *AJ*, 118, 1406
 Majewski, S. R., Skrutskie, M. F., Weinberg, M. D. & Ostheimer, J. C. 2003, *ApJ*, 599, 1082
 Martin, N. F., Ibata, R. A., Bellazzini, M., Irwin, M. J., Lewis, G. F., & Dehnen, W. 2004, *MNRAS*, 348, 12
 Martin, N. F., de Jong, J. T. A. & Rix, H.-W., 2008, *ApJ*, 684, 1075
 Momany, Y., Zaggia, S. R., Gilmore, G., Piotto, G., Carraro, G., Bedin, L. R. & de Angeli, F. 2006, *A&A*, 451, 515
 Newberg, H. J., et al. 2002, *ApJ*, 569, 245
 Padmanabhan, N., Schlegel, D. J., Finkbeiner, D. P., Barentine, J. C., Blanton, M. R., et al. 2008, *ApJ*, 674, 1217
 Pier, J.R., Munn, J.A., Hindsley, R.B., Hennessy, G.S., Kent, S.M., Lupton, R.H., & Ivezić, Z. 2003, *AJ*, 125, 1559
 Reylé, C., Marshall, D. J., Robin, A. C. & Schultheis, M. 2009, *A&A*, 495, 819
 Salpeter, E. E. 1955, *ApJ*, 121, 161
 Schlegel, D., Finkbeiner, D. & Davis, M. 1998, *ApJ*, 500, 525
 Sesar, B., et al. *AJ*, 134, 2236
 Sesar, B., Ivezić, Z., Grammer, S. H., Morgan, D. P., Becker, A. C., Jurić, M., De Lee, N., Annis, J., et al. 2010, *ApJ*, 708, 717
 Siegel, M. H., Majewski, S. R., Reid, I. N. & Thompson, I. B., 2002, *ApJ*, 578, 151
 Skrutskie, M. F., et al. 2006, *AJ*, 131, 1163
 Smith, J. A., et al. 2002, *AJ*, 123, 2121
 Stoughton, C. et al. 2002, *AJ*, 123, 485
 Tucker, D., et al. 2006, *AN*, 327, 821
 Vallée, J. P., 2008, *AJ*, 135, 1301
 Watkins, L. L., Evans, N. W., Belokurov, V., Smith, M. C., Hewett, P. C., Bramich, D. M., Gilmore, G. F., Irwin, M. J., et al. 2009, *MNRAS*, 398, 1757
 Yanny, B., et al. 2003, *ApJ*, 588, 824
 Yanny, B., Rockosi, C., Newberg, H. J., Knapp, G. R., Adelman-McCarthy, J. K., et al. 2009a, *AJ*, 137, 4377
 Yanny, B., Newberg, H. J., Johnson, J. A., Lee, Y. S., Beers, T. C., Bizyaev, D., Brewington, H., Re Fiorentin, P., et al. 2009b, *ApJ*, 700, 1282
 York, et al. 2000, *AJ*, 120, 1579
 Younger, J. D., Besla, G., Cox, T. J., Hernquist, L., Robertson, B., & Willman, B., 2008, *ApJ*, 676, L21